Submitted, accepted and published in Nanoscale 2013, **5**, 10189; DOI: 10.1039/C3NR02822D

Reduced graphene oxide: Firm support for catalytically active palladium nanoparticles and game changer in selective hydrogenations

Manuela Cano,[a] Ana M. Benito,[a] Esteban P. Urriolabeitia,[b] Raul Arenal,[c,d] and Wolfgang K. Maser*[a]

*[a] *Instituto de Carboquímica ICB-CSIC, C/Miguel Luesma Castán, E-50018 Zaragoza, Spain.*

Fax: +34 976 73 33 18; Tel: +34 976 73 39 77; E-mail: wmaser@icb.csic.es

[b]*Instituto de Síntesis Química y Catálisis Homogénea (ISQCH), CSIC-Univ. Zaragoza, C/ Pedro Cerbuna 12, E-50009 Zaragoza, Spain.*

[c]*LMA-INA, Univ. Zaragoza, C/Mariano Esquillor, E-50018 Zaragoza, Spain*

[d]*Fundacion ARAID, C/María de Luna 11, E-50018 Zaragoza, Spain*

Simultaneous decomposition and reduction of a Pd^{2+} complex in the presence of graphene oxide (GO) lead to the formation of Pd^0-nanoparticles (Pd-NPs) with average sizes of 4 nm firmly anchored on reduced graphene oxide (RGO) sheets. The Pd-NPs/RGO hybrids exhibited remarkable catalytic activity and selectivity in mild hydrogenation reactions where acidic properties of RGO play an active role and may act as important game-changer.

The development of novel catalyst systems for the sustainable and efficient modification of organic entities is one of the most challenging tasks in modern chemistry.[1] Heterogeneous catalysts based on palladium are of increased interest.[1b, 2] Available as nanoparticles (NPs) highest activities are achieved due to the enhanced fraction of catalytic Pd surface atoms.[3] Thus current synthesis routes tend to exploit approaches, which maximise a uniform nanoparticles' size distribution by minimizing

undesirable agglomeration effects. Here the use of support materials is one important concept to obtain stable and quite uniformly distributed Pd nanoparticles. Especially carbon based nanostructures with their high specific surface area and superior chemical stability, such as carbon nanotubes,[4] and most recently, graphene and its derivatives[5] have been used as support to obtain catalytically active Pd-NP/nanocarbon hybrid materials.

However, most of the synthesis approaches for these types of catalysts involve tedious multi-step reactions, such as the pre-functionalization of the carbon support,[6] the use of Pd stabilizers,[7] intercalation-exchange reactions,[5c] secondary reducing agents,[5d] etc. Recently we developed a facile and rapid method based on the in-situ decomposition of an organometallic Pd precursor in presence of multi-walled carbon nanotubes resulting in Pd-NPs of uniform size firmly attached to the nanotubes.[4f] The resulting Pd-NP/MWCNT hybrid material showed impressive catalytic activity on C-C coupling reactions including the full recovery of the catalyst. Being of generic character, this successful in-situ synthesis strategy should be easily transferred and adapted to graphene-based systems.

We here report on a facile one-pot in-situ synthesis approach to obtain Pd-NPs with average size of 4 nm firmly attached to reduced graphene oxide (RGO), favored by oxygen functionalities of the initial GO sheets. The resulting Pd-NP/RGO hybrid material was employed for the first time as heterogeneous catalyst in hydrogenation reactions of a variety of olefinic substrates. Obtaining high catalytic activities and selectivity under very mild reaction conditions these novel catalyst systems reveals that both Pd-NPs and the RGO support itself play critical roles in the catalytic process. The acid properties of remaining oxygen functionalities on the RGO sheets are key to selectively tune the overall hydrogenation process. RGO based catalysts thus may open

up new possibilities towards improved hydrogenation reactions.

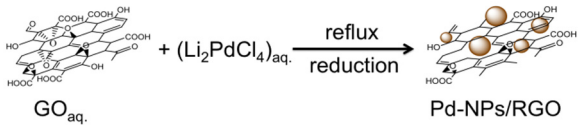

Scheme 1. One-pot *in-situ* reaction for synthesis of Pd-NPs/RGO.

The synthesis of the Pd-NP/RGO hybrid materials was carried out in aqueous medium. In the presence of graphene oxide (GO) a Pd precursor complex was decomposed and reduced in an *in-situ* one-pot reaction (Scheme 1). Employing GO and $Li_2[PdCl_4]$ in a 1:1 weight ratio and using hydrazine as the reducing agent (synthesis details are given in SI†) a Pd-NP/RGO hybrid material with a Pd loading of 34 wt.% was obtained. This corresponds to a palladium deposition yield of 85 % underlining the high efficiency of the applied synthesis route. Losses are related to: (i) removal of Pd not attached to RGO, estimated to be about 10-30 wt.% of initial Pd as observed in the case of MWCNTs,[4f] and (ii) removal of carbon and functional groups belonging to GO, being about 25-30 wt.% of initial GO as typically observed in hydrazine reduction processes of GO.[8] Less efficient results were obtained for syntheses based on the in-situ decomposition of precursor $Pd_2(dba)_3CHCl_3$ (see SI†).

Transmission electron microscopy (TEM) images of the synthesized Pd-NP/RGO material (Figure 1 a-c) clearly reveal highly exfoliated RGO sheets of 1 μm average lateral size homogeneously covered by finely dispersed and highly crystalline Pd nanoparticles of 4 nm in average size (see SI†).

The X-Ray diffractogram (Figure 1d) is dominated by a set of three strong peaks at 2q angles of 40º, 47º and 68º, indicative of Pd nanoparticles crystallized in a face-centred cubic structure. In addition, a broad peak of very low intensity at about 26 º reveals the presence of few-layered RGO, evolved from the initial GO support during the applied

hydrazine reduction treatment. Please note that the initial GO support is characterized by a diffraction peak at 10.6º (Figure 1d inset), indicative of a high interlayer spacing of 0.83 nm caused by the presence of oxygenated functional groups and trapped water molecules. Upon reduction these groups and molecules are removed thus leading to a decrease in the interlayer spacing evidenced by the appearance of the diffraction peak at 26º.[8] Moreover, the absence of diffraction peaks of PdO further suggests that the reduction of palladium, initially present in the precursor salt as Pd^{2+}, successfully was achieved in the applied one-pot decomposition/reduction process.

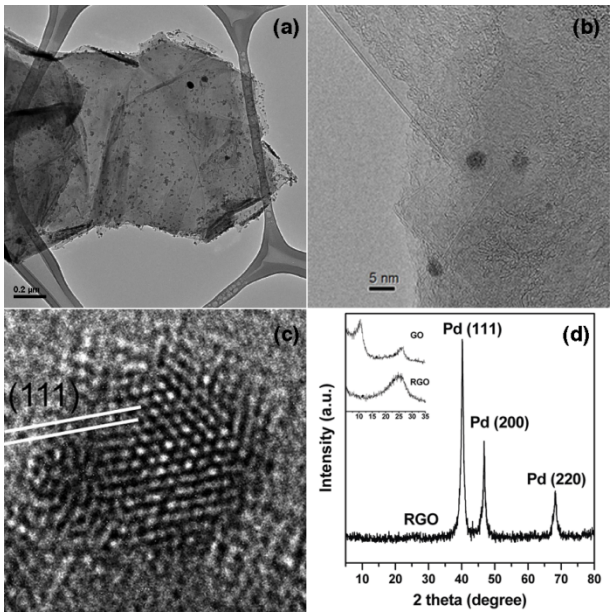

Fig. 1 (a, b) TEM images of sheets of RGO covered with Pd NPs; (c) HRTEM image of Pd NP on RGO; (d) XRD of Pd-NPs/RGO. Inset: GO and RGO.

The simultaneous reduction of graphene oxide and Pd^{2+} was further examined by XPS (Figure 2a-c). C1s core level spectrum of GO shows a strong peak at 284.5 eV, corresponding to sp^2 carbon (C-C), accompanied by a prominent peak at 286.8 eV, indicative of C-O bonds, and followed by two smaller peaks at 288.3 eV and 289.49 eV

assigned to C=O and O-C=O groups, respectively. It becomes clear that initial GO is characterized by a large amount of functional oxygen groups with a calculated C/O ratio of 2.65. On the other hand, the XPS C1s spectrum of the Pd-NP/RGO hybrid material shows a significant reduction of the amount of oxygen functional groups with an increased C/O value of 8.4, as a consequence of the applied hydrazine reduction process. The fact that this C/O value is lower than one would expect for the reduction of GO alone[8] suggests that competing reduction processes, simultaneously acting on GO and Pd^{2+}, are taking place. Indeed, the Pd 3d XPS spectrum of the Pd-NP/RGO hybrid material exhibiting the typical bands for Pd $3d_{3/2}$ (338.3 eV) and $3d_{5/2}$ (333.0 eV), confirms that Pd is effectively reduced into the Pd^0 oxidation state, in agreement with the bulk data from X-ray diffraction. The additional existence of a minor Pd^{2+} component (25%), as revealed by deconvolution of the Pd 3d core level spectrum, most likely relates to the oxidized surface layer of Pd nanoparticles being in direct contact with functional defect sites of the RGO support. Apparently, at the initial state of precursor decomposition Pd^{2+} NPs chemically interact with the oxygen functional groups of GO by forming Pd-O linkages, facilitated by the highly electrophilic character of Pd^{2+}. These linkages then provide heterogeneous nucleation sites on which the Pd^0 NPs form upon reduction. This may explain the efficient and firm anchoring of the Pd nanoparticles on RGO, in a similar way as recently described for Pt nanoparticles supported on GO.[9] Furthermore, the initial anchoring of Pd to existing defect sites, significantly reduces the metal mobility, which is significant on smooth graphene surfaces,[10] and thus avoids agglomeration and contributes to the retention of fine particles on the RGO support (see SI† for the case of RGO and MWCNTs).

The simultaneous reduction of graphene oxide and Pd^{2+} was further examined by XPS (Figure 2a-c). C1s core level spectrum of GO shows a strong peak at 284.5 eV,

corresponding to sp^2 carbon (C-C), accompanied by a prominent peak at 286.8 eV, indicative of C-O bonds, and followed by two smaller peaks at 288.3 eV and 289.49 eV assigned to C=O and O-C=O groups, respectively. It becomes clear that initial GO is characterized by a large amount of functional oxygen groups with a calculated C/O ratio of 2.65. On the other hand, the XPS C1s spectrum of the Pd-NP/RGO hybrid material shows a significant reduction of the amount of oxygen functional groups with an increased C/O value of 8.4, as a consequence of the applied hydrazine reduction process. The fact that this C/O value is lower than one would expect for the reduction of GO alone[8] suggests that competing reduction processes, simultaneously acting on GO and Pd^{2+}, are taking place. Indeed, the Pd 3d XPS spectrum of the Pd-NP/RGO hybrid material exhibiting the typical bands for Pd $3d_{3/2}$ (338.3 eV) and $3d_{5/2}$ (333.0 eV), confirms that Pd is effectively reduced into the Pd^0 oxidation state, in agreement with the bulk data from X-ray diffraction. The additional existence of a minor Pd^{2+} component (25%), as revealed by deconvolution of the Pd 3d core level spectrum, most likely relates to the oxidized surface layer of Pd nanoparticles being in direct contact with functional defect sites of the RGO support. Apparently, at the initial state of precursor decomposition Pd^{2+} NPs chemically interact with the oxygen functional groups of GO by forming Pd-O linkages, facilitated by the highly electrophilic character of Pd^{2+}. These linkages then provide heterogeneous nucleation sites on which the Pd^0 NPs form upon reduction. This may explain the efficient and firm anchoring of the Pd nanoparticles on RGO, in a similar way as recently described for Pt nanoparticles supported on GO.[9] Furthermore, the initial anchoring of Pd to existing defect sites, significantly reduces the metal mobility, which is significant on smooth graphene surfaces,[10] and thus avoids agglomeration and contributes to the retention of fine particles on the RGO support (see SI† for the case of RGO and MWCNTs).

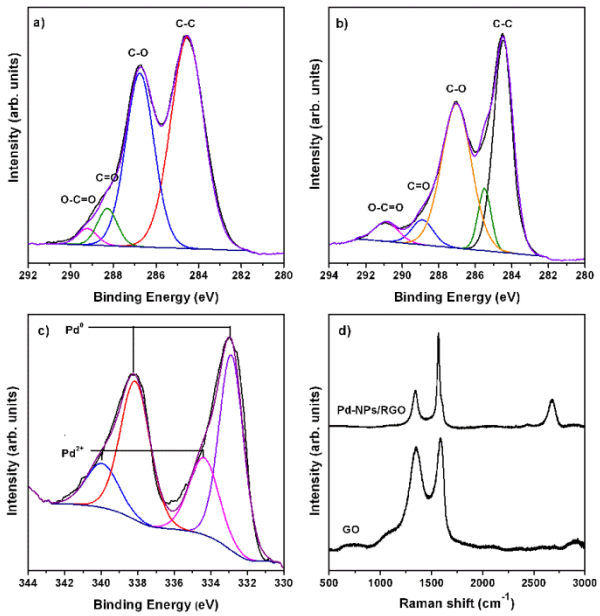

Fig. 2 XPS spectra of (a) GO (C1s), (b) Pd-NPs/RGO (C1s), (c) Pd-NPs/RGO (3d). (d) Raman spectra of GO and Pd-NPs/RGO.

Raman spectroscopy (Figure 2d) ones more corroborates the effective reduction of GO to RGO in the one-pot synthesis process of Pd-NP/RGO. The spectrum is dominated by a strong G-band at 1590 cm^{-1}, related to graphene sheet in-plane C-C vibrations of the sp^2 carbon, accompanied by a D-band at about 1350 cm^{-1}, characteristic for the presence of defects and disorder in the graphene plane. While for GO itself the intensity of the D-band is almost comparable to the G-band in case of the Pd-NP/RGO material its intensity is significantly reduced by a factor of 2.5. This is a direct hint for the loss of initial functional groups on GO and an enhanced sp^2 character, further evidenced by the appearance of the so-called 2D band at about 2700 cm^{-1}.[1, 8, 11]

All these results consistently demonstrate the high efficiency of the applied facile and straightforward one-pot in-situ decomposition-reduction process in order to achieve a high loading of Pd^0 nanoparticles well-dispersed and firmly supported on RGO.

With a specific surface area of 315 m^2/g (see SI†) the Pd-NP/RGO hybrid material containing 34 wt.% of Pd is of great interest for catalytic applications. Therefore, in a

next step, it was evaluated as catalyst in hydrogenation reactions of a wide array of olefinic substrates, more specifically α,β-unsaturated ketones, alkenes, cyclic di-, tri- and tetraenes, aromatic compounds, terpenes and terpenoids. The overall reaction conditions are described in detail in Supporting Information. It is worthwhile mentioning that all reactions were successfully carried out at 1 atm and 25 ºC, i.e. under very mild conditions, clearly differing from the high pressure and high temperature processes usually needed for the hydrogenation of the mentioned substrates.[12] Results of the hydrogenation reactions are summarized in Table 1 and are commented in the following. Please note that no hydrogenation activity was observed in these reactions using RGO alone without the presence of Pd. This is in contrast to a recent report suggesting that RGO is catalytically active for the case of nitrobenzene,[13] but completely ignoring the likely influence of the employed hydrogenation agent hydrazine hydrate itself.[14]

Hydrogenation of acetophenone (AP) with the required amount of hybrid to contain 1% Pd as catalyst resulted after 4h in a low yield of a mixture enriched in 1-phenylethanol (PE), with small amounts of ethylbenzene (EB). The preferred formation of PE, an important synthon for the elaboration of fine chemicals,[15] provides special interest in the use of the Pd-NP/RGO hybrid material as catalyst towards a selective PE production. Attempts to further tune the competing hydrogenations towards PE were unsuccessful. Instead, optimization towards EB production could be achieved on cost of PE. Increasing the amount of Pd catalyst to 2% (mmol) by keeping the reaction time roughly constant selectively forces the reaction towards EB with an overall TOF value of 8 h^{-1}. The selective hydrogenation towards EB not only is clearly different to what usually is obtained with other types of Pd supported catalysts, such as Pd/Al_2O_3[16] and Pd-NP/MWCNTs[17], but moreover, clearly suggests a critical role of RGO itself in

hydrogenation processes as explained in the following. The direct hydrogenation of AP towards EB takes place in a first step by hydrogenation of AP to PE, catalyzed by Pd. This is followed in a second step by the acid-catalyzed dehydration of PE to styrene,[16b] facilitated by RGO. Subsequently, in a final third step, styrene is hydrogenated to EB, again catalyzed by Pd. (see Scheme 2).

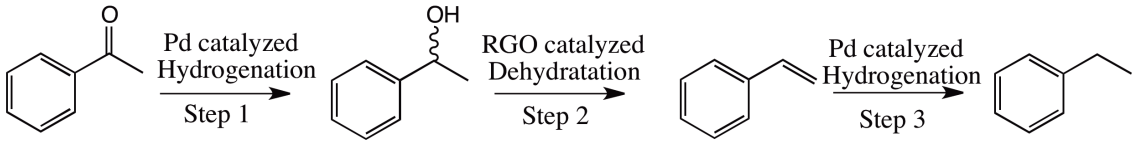

Scheme 2. Hydrogenation process of acetophenone

While this last conversion step is enhanced for higher amounts of Pd (see table 1), the compulsory existence of the intermediate product styrene must be directly related to the presence of the remaining functional oxygen groups of the RGO substrate (see XPS results above) providing the essential acidic formation conditions. Although RGO itself does not show hydrogenation activity its remaining functional oxygen groups assist catalytic processes, which only occur under acidic conditions. As for the case described, RGO thus may act as an active game-changer in Pd catalyzed hydrogenation processes and thus directly contributes to achieve enhanced selectivity.

Hydrogenation of cyclohexene proceeds smoothly using very low amounts of Pd catalyst (0.1 mmol %), giving cyclohexane with yields of about 50 %, being lower when compared to the use of MWCNTs as support.[17] More interestingly, the hydrogenation of 1,3,5,7-cyclooctatetraene (COT) afforded selectively the partially hydrogenated product cyclooctene (COE) in very good yields and short reaction times, slightly better when comparing to the use of MWCNTs as support.[17] Although several

authors report on the determination of the heat of hydrogenation of COT[18], the selective Pd-catalysed hydrogenation of COT to COE has rarely reported so far[17,19], a fact probably based on the general consideration that COT is the most difficult to hydrogenate C8 polyolefine.[20]

Table 1 Summary of hydrogenation reactions

Substrate	Pd amount[a,b] (%)	Time (h)	Product	Yield[c] (%)	TOF[d] (h^{-1})
Acetophenone	1	4	Ethylbenzene	2 (EB)	
			1-Phenylethanol	14 (PE)	3.5
	2	3.5	Ethylbenzene	56	8
Cyclohexene	0.1	19	Cyclohexane	50	26
Cycloocta-tetraene	1	2	Cyclooctene	100	50
	2.5	5	Cycloheptane	100	8
Cyclo-heptatriene	0.5	1.75	Cycloheptene	21	24
	0.5	3.75	Cycloheptene	63	33
Limonene	0.5	19	*p*-Menthanes	6+6	--
			p-Menthene	11	

[a]Pd in Pd-NP/RGO catalyst (in mmol) with respect to amount of substrate (in mmol) expressed in %. [b]Use of RGO without Pd does not lead to hydrogenation activity. [c]Isolated yield. [d]TOF: Product (mmol) / [Pd (mmol) x Time (h)].

Even more remarkable is the Pd-catalysed hydrogenation of 1,3,5-cycloheptatriene, which has been scarcely investigated using Pd-borides[21] or most recently by employing Pd-NPs supported on MWCNTs.[17] As can be seen from Table 1, by only changing the

amount of catalyst it is possible to control the target-hydrogenated product. While Pd in a concentration of 2.5 mmol% affords the fully hydrogenated derivative cycloheptane with a yield of 100 %, a concentration of 0.5 mmol% of Pd selectively results in cycloheptene in similar reaction times, albeit with a reduced yield of 21 %. Selectivity towards cycloheptane is comparable to results from Pd-NP/MWCNT catalysts,[17] while the one towards cycloheptene is somewhat lower. However, since the used Pd amounts and reaction times are not identical a direct comparison is not possible yet. Due to the interest of cycloheptene as raw material in organic chemistry and monomer in polymer synthesis, a further optimization was attempted. By increasing the reaction time from 1.75 h to 3.75h cycloheptene was selectively obtained with a significantly enhanced yield of 63 %.

Furthermore, we also carried out the hydrogenation of a naturally occurring product, namely *R*-(+)-limonene, a cyclic terpene. For all the various different conditions employed, only low product yields were achieved. A representative example is shown in Table 1. Interestingly, the reaction occurred with a notable degree of selectivity, affording only three products: the two fully hydrogenated diastereoisomers of *p*-menthane (cis and trans) and the partially hydrogenated *p*-menthene. Usually up to six different products can be observed upon the hydrogenation of limonene using Pd supported on activated carbon as well as on Al_2O_3,[22] while four products are reported for Pd-NP/MWCNT catalysts.[17] The cis/trans isomers appear in an almost equimolar ratio, as usually observed, and, accidentally, the molar ratio *p*-menthene/*p*-menthane is 1. Attempts to further improve the selectivity of this reaction towards the production of *p*-menthene yet were not accomplished.

Finally, recyclability studies were carried out for the hydrogenation reaction of cycloheptatriene (see SI for experimental conditions). Results shown in Table 2 reveal

that the catalyst remains fully active during four complete cycles while also maintaining its selective conversion to cycloheptane up to the third cycle. Full recovery of Pd after the fourth cycle demonstrates that no leaching occurs. This further confirms the firm anchoring of Pd NPs on the RGO sheets and, being incompatible with the formation of larger-sized Pd aggregates eventually causing a reduced hydrogenation activity, proves the efficiency of Pd-NP/RGO catalyst systems.

Table 2 Reuse of Pd-NP/RGO catalyst in the hydrogenation of 1,3,5-cycloheptatriene

Run (Number)	1	2	3	4
Yield (%)	100	100	100	100
Conversion (%)	100	100	100	80% Cycloheptane 20% Cycloheptene
Pd recovery[a] (%)	--	--	--	100

[a]Percentage of Pd retained after run 4 with respect to initial sample as determined by ICPS technique

Summarizing, a new catalyst system based on palladium nanoparticles of 4 nm average size firmly anchored on RGO was prepared by simultaneous decomposition/reduction of $Li_2[PdCl_4]$ in the presence of GO in a simple one-pot procedure. For the first time a straightforward synthesis route towards graphene-based nanohybrids is presented, which fully profits from the oxygen functionalities of GO sheets and its reduction possibilities thus avoiding tedious pre-functionalization steps. The resulting Pd-NP/RGO hybrid material proved to be a highly versatile and effective hydrogenation catalyst under mild reaction conditions for a wide range of olefinic

substrates. High selectivity and remarkable activity were achieved. The RGO support itself through its acidic properties of remaining oxygen functionalities may actively interfere in the overall hydrogenation process and take over the role of a game changer contributing to achieve enhanced selectivity of specific products in Pd catalyzed processes. Facile synthesis as well as efficient and selective hydrogenation performance thus underline the promising potential of graphene oxide for the development of functional graphene-based nanohybrids for catalytic applications and beyond.

Acknowledgements

Financial support from Spanish MINECO (projects MAT2010-15026 and CTQ2011-22589), CSIC (project 201080E123), and DGA-ESF (T66N,E-97, and E-26) is gratefully acknowledged.

References

1 (a) I. T. Horváth and P. T. Anastas, *Chem. Rev.*, 2007, **107**, 2169; (b) M. J. Climent, A. Corma and S. Iborra, *Chem. Rev.*, 2011, **111**, 1072.

2 J. Tsuji, *Palladium reagents and catalysts: New perspectives for the 21st century*, J. Wiley & Sons, 2004.

3 (a) D. Astruc, *Nanoparticles and Catalysis*, Wiley VCH, 2008; (b) I. Favier, D. Madec, E. Teuma and M. Gomez, *Curr. Org. Chem.*, 2011, **16**, 3127.

4 (a) P. Serp, M. Corrias and P. Kalck, *Appl. Catal. A: Gen.*, 2003, **253**, 337; (b) P. Serp and E. Castillejos, *ChemCatChem*, 2010, **2**, 41; (c) N. Karousis, G.-E. Tsotsou, F. Evangelista, P. Rudolf, N. Ragoussis and N. Tagmatarchis, *J. Phys. Chem. C*, 2008, **112**, 13463; (d) I. Sayago, E. Terrado, E. Lafuente, M. C. Horrillo, W. K. Maser, A. M. Benito, R. Navarro, E. P. Urriolabeitia, M. T. Martinez and J.

Gutierrez, *Synth. Met.*, 2005, **148**, 15; (e) A. Ansón, E. Lafuente, E. Urriolabeitia, R. Navarro, A. M. Benito, W. K. Maser and M. T. Martínez, *J. Phys. Chem. B*, 2006, **110**, 6643; (f) M. Cano, A. M. Benito, W. K. Maser and E. P. Urriolabeitia, *Carbon*, 2011, **49**, 652.

5 (a) P. Xi, F. Chen, G. Xie, C. Ma, H. Liu, C. Shao, J. Wang, Z. Xu, X. Xu and Z. Zeng, *Nanoscale*, 2012, **4**, 5597; (b) M. Önder, E. Kayhan, Ö. Saim and J. J. Schneider, *Int. J. Hydrogen Energy*, 2012, **37**, 8161; (c) G. M. Scheuermann, L. Rumi, P. Steurer, W. Bannwarth and R. Mühlhaupt, *J. Am. Chem. Soc.*, 2009, **131**, 8262; (d) J. Yang, C. Tian, L. Wang, T. Tan and J. Yin, *ChemPlusChem*, 2012, **77**, 301.

6 (a) J.-J. Shi, G.-H. Yang and J.-J. Zhu, *J. Mater. Chem.*, 2011, **21**, 7343; (b) Y. Zhao, L. Zhan, J. Tian, S. Nie and Z. Ning, *Electrochim. Acta*, 2011, **56**, 1967; (c) G. M. Neelgund and A. Oki, *Appl. Catal. A: Gen.*, 2011, **399**, 154; (d) M. R. Nabid, Y. Bide and S. J. Tabatabaei Rezaei, *Appl. Catal. A: Gen.*, 2011, **406**, 124.

7 Y. Li, X. Fan, J. Qi, J. Ji, S. Wang, G. Zhang and F. Zhang, *Nano Res.*, 2010, **3**, 429.

8 C. Vallés, J. D. Núñez, A. M. Benito and W. K. Maser, *Carbon*, 2011, **50**, 835.

9 C. Nethravathi, E. A. Anumol, M. Rajamathi and N. Ravishankar, *Nanoscale*, 2011, **3**, 569.

10 J. A. Rodríguez-Manzo, O. Cretu and F. Banhart, *ACS Nano*, 2010, **4**, 3422.

11 (a) A. C. Ferrari, *Solid State Commun.*, 2007, **143**, 47; (b) R. Arenal, *Appl. Phys. Lett.*, 2007, **91**, 211903; (c) R. Arenal, G. Montagnac, P. Bruno and D. M. Gruen, *Phys. Rev. B,* 2007, **76**, 245316.

12 J. A. Anderson, A. Athawale, F. E. Imrie, F. M. McKenna, A. McCue, D. Molyneux, K. Power, M. Shand and R. P. K. Wells, *J. Catal.* 2010, **270**, 9.

13 Y. Gao, D. Ma, C. Wang, J. Guan and X. Bao, *Chem. Comm.*, 2011, **47**, 2432.

14 J. W. Larsen, M. Freund, K. Y. Kim, M. Sidovar and J. L. Stuart, *Carbon*, 2000, **38**, 655.

15 R. Noyori and T. Ohkuma, *Angew. Chem. Int. Ed.*, 2001, **40**, 40.

16 (a) A. Drelinkiewicza, A. Waksmundzka, W. Makowski, J. W. Sobczak, A. Król and A. Zieba, *Catalysis Letters*, 2004, **94**, 143; (b) P. Mäki-Arvela, S. Sahin, N. Kumar, T. Heikkilä, V.-P. Lehto, T. Salmi and D. Y. Murzin, *J. Mol. Catal. A: Chemical*, 2008, **285**, 132.

17 M. Cano, A. M. Benito, W. K. Maser and E. P. Urriolabeitia, *New J. Chem.*, 2013. **37**, 1968.

18 D. W. Rogers, *J.Mol. Struct.*, 2000, **556**, 207.

19 M. Seefelder and W. Raskob, *US Patent*, 1966, 3251892.

20 H. A. Tayim and J. C. Bailar, *J. Am. Chem.l Soc.*, 1967, **89**, 4330.

21 B. D. Polkovnikov, O. M. Nefedov, E. P. Mikos and N. N. Novitskaya, *Russ. Chem. Bull.*, 1968, **17**, 1175.

22 R. J. Grau, P. D. Zgolicz, C. Gutierrez and H. A. Taher, *J. Mol. Catal. A: Chemical*, 1999, **148**, 203.

† Supplementary Information (SI†) available: [Synthesis and Results].

Supplementary Information

Reduced graphene oxide: Firm support for catalytically active palladium nanoparticles and game changer in selective hydrogenations

Manuela Cano[a], Ana M. Benito[a], Esteban P. Urriolabeitía[b], Raul Arenal[c,d] and Wolfgang K. Maser[*a]

[a]ICB-CSIC, E-50018 Zaragoza, Spain. [*]wmaser@icb.csic.es
[b]ISQCH-CSIC-Univ. Zaragoza, E-50009 Zaragoza, Spain
[c]LMA-INA-Univ. Zaragoza, E-50018 Zaragoza, Spain
[d]Fundacion ARAID, Zaragoza, E-50018 Zaragoza, Spain

S1. Experimental

S1.1 Materials

All reagents and solvents were obtained from Sigma-Aldrich Co., St. Louis, MO, USA).

S1.2 Preparation of graphite oxide, graphene oxide and reduced graphene oxide

(a) Graphite oxide was prepared, using a modified Hummers' method, from graphite powder by oxidation with $NaNO_3$, H_2SO_4 and $KMnO_4$ in an ice bath as reported in detail elsewhere;[1, 2] (b) A suspension of graphene oxide (GO) sheets was prepared as reported elsewhere.[3, 4] In brief, the prepared graphite oxide powder was sonicated in distilled water (1 mg/mL) for 2 hours, followed by mild centrifugation of the suspension at 4500 rpm for 60 min. The separated brown-coloured supernatant water GO dispersion had a concentration of 0.35 mg/mL. (c) Reduced graphene oxide (RGO) was prepared by adding an excess of hydrazine hydrate $N_2H_4{\cdot}H_2O$ (900 µL) to the GO dispersion and stirred under reflux for 5 hours. Filtration through a polycarbonate membrane filter of 3 µm pore size, followed by washing with 200 mL of distilled water and vacuum drying at 80 ˚C for 48 afforded the powder-like RGO material.

S1.3 Preparation of palladium precursor dilithiumtetrachloropalladate(II) $Li_2[PdCl_4]$

$PdCl_2$ (23 mg, 0.13mmol) was suspended in water (5 mL). LiCl was added in excess (27 mg), 0.5 mmol). The resulting mixture was refluxed for 1 hour until complete dissolution of the palladium salt, affording a clear deep-red $Li_2[PdCl_4]$ solution (34 mg, 0.13 mmol)

S1.4 Preparation of Pd-NP/RGO hybrid material using $Li_2[PdCl_4]$ precursor

GO was reacted with $Li_2[PdCl_4]$ in a 1:1 weight percent ratio as follows: 100 mL of the prepared GO solution (containing 35 mg of GO) was added to the prepared $Li_2[PdCl_4]$ solution (containing 35 mg of the complex). The resulting $Li_2[PdCl_4]$/GO mixture was reflux heated under stirring for 1.5 hours. Subsequently, an excess of hydrazine hydrate $N_2H_4{\cdot}H_2O$ (900 μL) was added to the hot suspension. Stirring under reflux continued for an additional 5 hours before the suspension was allowed to cool down to room temperature. Filtration through a polycarbonate membrane filter of 3 μm pore size, followed by washing with 200 mL of distilled water and vacuum drying at 80 ˚C for 48 afforded the powder-like Pd-NP/RGO material containing 34 wt.% of Pd. This material was used for further characterization and subsequent hydrogenation reactions. In the same way, “low-loading” catalysts were prepared using GO : $Li_2[PdCl_4]$ weight ratios of 10:1 and 20:1. The resulting Pd-NP/RGO hybrid materials contained 12.6 wt.% and 2.6 wt.% of Pd, respectively.

S1.5 Preparation of Pd-NPs/RGO hybrid material using [$Pd_2(dba)_3CHCl_3$]precursor

In previous communications[5, 6] we reported that the reaction of MWCNTs with the palladium complex [$Pd_2(dba)_3{\cdot}CHCl_3$] (dba = dibenzylideneacetone) using reflux or microwave techniques afforded the hybrid material Pd-NPs/MWCNTs with high loading of Pd (up to 40 wt.%) in reaction times ranging from 2 h (reflux) to few minutes (microwaves). In an analogous way we reacted here RGO and [$Pd_2(dba)_3{\cdot}CHCl_3$] in a 1:1 ratio in dry toluene at 110 ºC affording Pd-NP/RGO hybrid material with a Pd load of only 5 wt.% for both, reflux and microwave heating process. With an efficiency of below 30%, this synthesis method was not considered any longer of practical interest for the preparation of Pd-NP/RGO materials employed in hydrogenation applications.

S1.6 Catalytic hydrogenation experiments

Hydrogenation experiments were carried out exclusively with the "high-loading" Pd-NP/RGO material containing 34 wt.% of Pd (please note: Since high- and low-loading hybrid materials are equally composed of small-sized nanoparticles (see below in S2) it is preferred to use the hybrid material with the maximum Pd loading thus avoiding the use of larger amounts of the overall hybrid material for the hydrogenation reactions). To this end, the palladium catalyst supported on RGO in the appropriate amount (see article Table 1), was dispersed in $CHCl_3$ (2 mL) under stirring in a 5 mL round-bottomed flask at room temperature and atmospheric pressure. To this suspension 1 mmol of the substrate to be hydrogenated was added. The system was then evacuated and backfilled with H_2 in cycles for at least five times. The pressure of H_2 was kept constant (p_{H2} = 1 atm) with a balloon system during the whole reaction time. Once the hydrogenation has been performed, the resulting suspension was filtered through a 3 μm pore

polycarbonate membrane filter, and the solid catalyst material was washed with CH_2Cl_2 and water, and dried at 110 °C overnight. The solvent was removed from the organic solution by fractional distillation, affording the hydrogenated products as oily residues, which were characterized by ^{1}H and ^{13}C NMR spectroscopy and the spectral data were compared with data from corresponding reference samples found in the literature data bases. Recyclability tests were performed for the case of 1,3,5-cycloheptatriene using 2.5% of Pd in the Pd-NP/RGO catalyst system and a hydrogenation time of 5h. Four consecutive reactions were carried out. After each run the catalyst was isolated by filtration, washed and dried before a new batch of reactant is added. Activity (product yield), selectivity (production conversion) were analyzed after each run by NMR technique as explained above. The amount of palladium retained was determined by ICPS after the final run.

S1.7. Characterization of the hybrid materials and hydrogenation products

The morphology of the prepared hybrid materials was studied by transmission electron microscopy (TEM, JEOL-2000 FXII working at 200 kV and a high-resolution Cs-corrected Titan-Cube microscope working at 80 kV). Samples were dispersed in ethanol in ultrasound bath for 10 min, and a drop of the suspension was placed onto a copper grid coated with carbon film. Powder X-ray diffraction (XRD) measurements were carried out at room temperature on a Bruker D8 Advance diffractometer using a Cu Kα X-ray radiation. Peak position and indexing was performed using Bruker TOPAS and EVA software packets. The metal loading in the carbonaceous samples was determined by Inductive coupled plasma spectroscopy (ICPS) using a Jobin-Yvon 2000 Ultrace Analyzer. X-ray photoelectron spectroscopy (XPS) was carried out on an ESCAPlus

Omicron spectrometer using a monochromatized Mg X-ray source (1253.6 eV). Data were analyzed using CasaXPS software packet. Raman spectra were recorded with a Horiba Jobin Yvon HR800 UV spectrometer using an excitation wavelength of 532 nm. BET specific surface area was calculated from nitrogen adsorption isotherms acquired at liquid nitrogen temperature on a Micromeritics ASAP 2010 adsorption apparatus. ^{1}H and ^{13}C NMR spectra of the hydrogenation products were taken in CD_2Cl_2, $CDCl_3$ or acetone-d_6 solutions at 25 °C on Bruker Avance-300 and Avance-400 spectrometers (δ, ppm; *J*, Hz), and referenced using the solvent signal as internal standard.

S2. Results

S2.1 TEM results for Pd-NP/RGO using $Li_2[PdCl_4]$ precursor

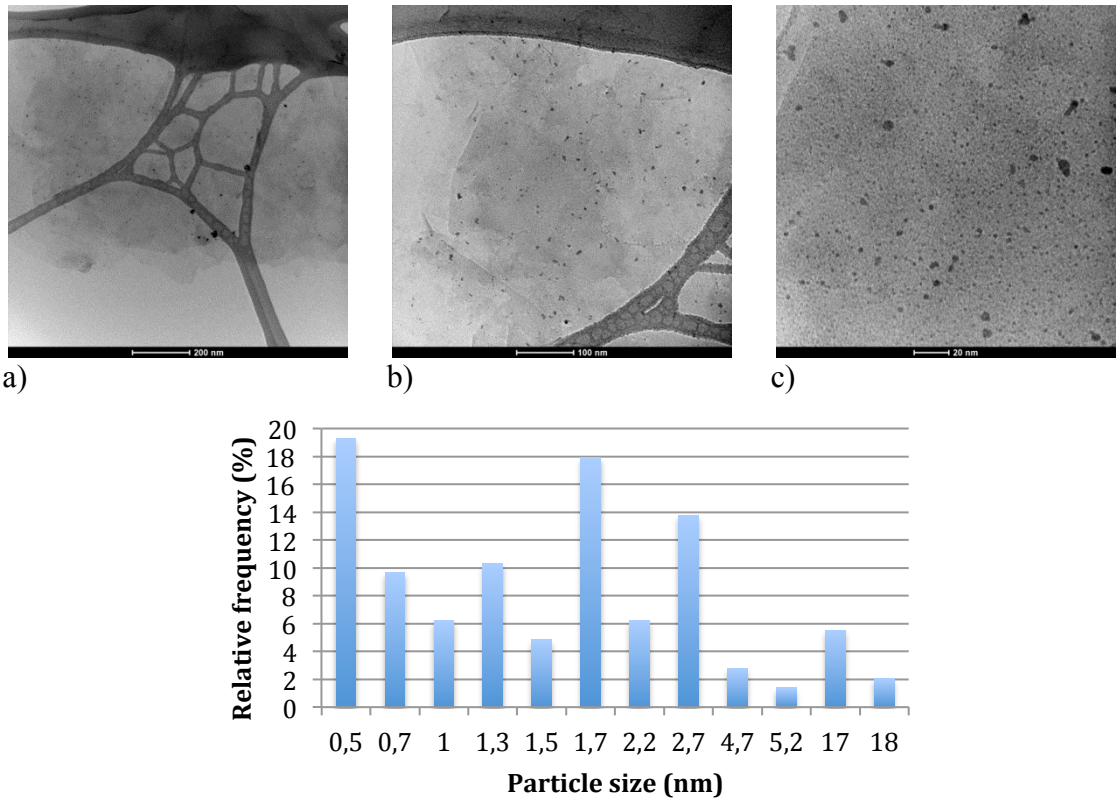

Figure S2.1. TEM images of hybrid materials synthesized from precursor $Li_2[PdCl_4]$ at three different areas and scales (a-c) and particle size distribution (d).

Figures S1 (a-c) shows TEM images of hybrid materials synthesized from precursor $Li_2[PdCl_4]$ at different scales. At highest magnification (c) a uniform distribution of small-sized nanoparticles in the range of 0.5 to 5 nm can be seen. These are accompanied by a significantly lower number of some larger-sized nanoparticles in the range of 18 nm. Very similar distributions can be seen in other areas (a,b). The larger magnification only should point out the rather homogeneous coverage of the RGO sheets. A typical particle size distribution is depicted in (d) obtained from evaluation of 145 particles on figure (c). Average particle size is about 3 to 4 nm. The presence of functional groups on the initial GO sheets may either favor the attachement

(electrostatic or covalent) of Pd nanoparticles or/and affect their mobility on an otherwise smooth surface, thus efficiently reducing the possibility for clustering into larger nanoparticles,[7, 8] as observed when using RGO sheets and metal complexes with Pd in the neutral state (see S2.2).

S2.2 TEM results for "low-loading" Pd-NP/RGO hybrids using $Li_2[PdCl_4]$ precursor

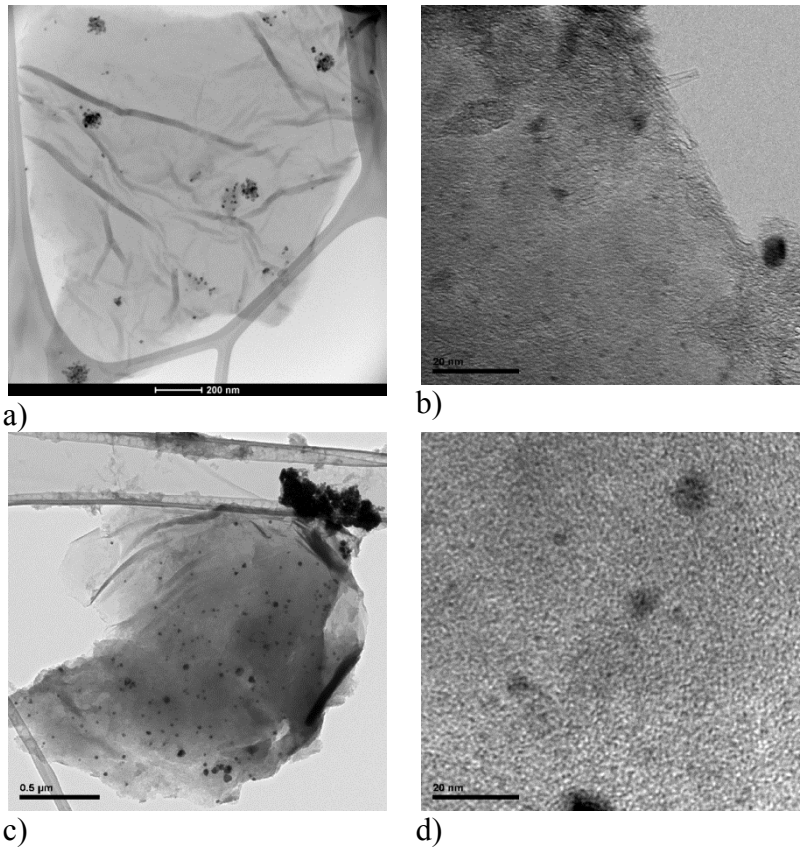

Figure S2.2. TEM images of hybrid materials synthesized form precursor $Li_2[PdCl_4]$. (a) and (b) GO: $Li_2[PdCl_4]$ 10:1 weight ratio at low and high magnification, respectively. (c) and (d) GO:$Li_2[PdCl_4]$ 20:1 weight ratio at low and high magnification, respectively.

TEM images of the "low-loading" Pd-NP/RGO hybrid materials (Figure S2.2) do not reveal esssential differences compared to the high-loading sample (Figure S1). At high magnification scales (Figure S2.2 b,d) Pd nanopatices of sizes below 10 nm easily can

be spotted throughout different areas of the sample. In addition, larger isolated Pd nanoparticles beyond 10 nm or even complete areas of larger Pd agglomerates can be observed at lower magnification (Figure S2.2 a,c). In this sense it is worthwhile to take into account the following consideration: While TEM, as a highly local technique, is of special value for the detection of small sized nanoparticles and their distribution no reliable information can be obtained concerning larger agglomerates of Pd nanoparticles, their sizes and their spatial distribution.

S2.3. XRD results for Pd-NP/RGO using $Li_2[PdCl_4]$ precursor

X-ray diffraction (XRD) as a bulk technique providing information on diffracting crystallite planes covers all different crystallite size domains. Applying the Debye-Scherrer equation, the average crystallite sizes can be determined from the FWHM of the diffraction peaks.[9] This is suitable for crystallite sizes in the range from 100 nm down to 10 nm. Below this value it is not applicable anymore. Providing selectively information on crystallite sizes above 10 nm XRD thus is a suitable technique to reveal the existence of larger agglomerated nanopaticles in the prepared Pd-NPs/RGO hybrid materials (while no information can be extracted on particle sizes below 10 nm).

Figure S2.3 shows the X-Ray powder diffractograms of the Pd-NP/RGO hybrid materials. For all the prepared concentrations, the diffraction peaks of Pd^0 can be clearly observed. The crystallite sizes applying the Debye-Scherrer equation are summarized in Table S2.1.

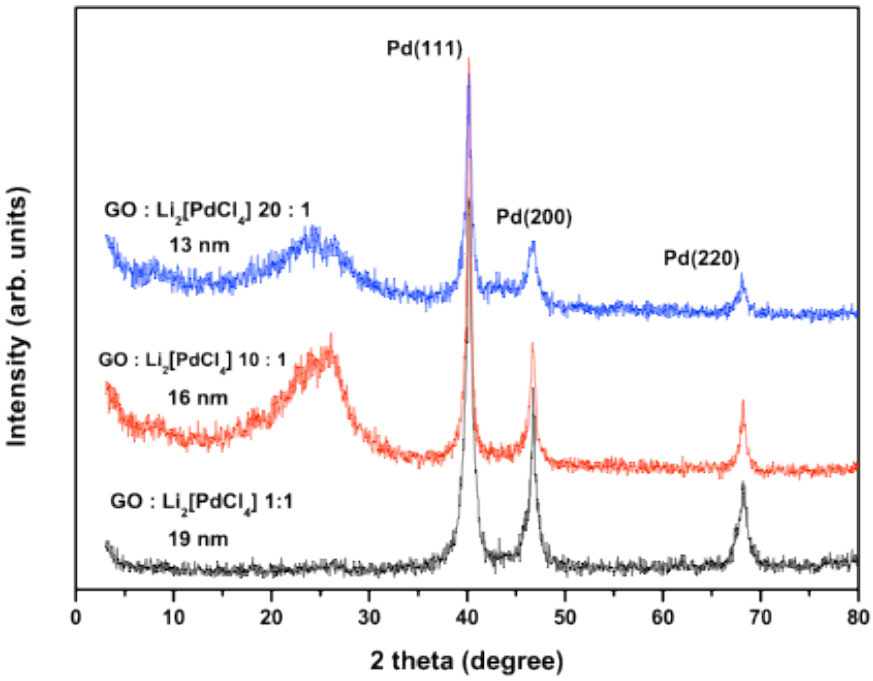

Figure S2.3. X-ray powder diffractograms of Pd-NP/RGO hybrids of different concentrations. Concentration and average crystallite size from Debye-Scherrer analysis are indicated.

Table S2.1. Crystallite size of Pd in the Pd-NP/RGO hybrid materials with different Pd loadings

GO : $Li_2[PdCl_4]$ weight ratio^{+}	**Pd loading (wt.%)**$^{++}$	**Crystallite size (nm)**$^{+++}$
1 : 1	34	19
10 : 1	12.5	16
20 : 1	2.5	11

$^{+}$used in synthesis. $^{++}$determined by ICPS. $^{+++}$determined by Debye-Scherrer formula

As can be seen from Table S2.1, the higher the Pd loading in the final hybrid material so larger the Pd crystallite size, and correspondingly the size of the individual Pd nanoparticles. The picture which emerges from XRD and TEM observations is the following: Pd nanoparticles of sizes in between 2 to 10 nm with average size of about 4 nm are obtained independently of the used Pd concentration. This again may underline important role of oxygen funtional groups of the starting GO material serving as nucleation points. Additionally at higher Pd concentrations larger Pd nanoparticles seem to form more likely.

S2.4. Mechanism for the formation of large-sized Pd nanoparticles

Two principal scenarios could be envisaged:

(a) Pd nanoparticles well-anchored by the functional oxygen groups of the initial GO support serve as nucleation points for continuous growth favored by enhanced Pd precursor concentrations. However, the experimental facts do not fully support this mechanism.

(b) Pd precursors which do not directly "find" functional oxygen group on the GO support maintain their high mobility and thus easily can form larger-sized nanoparticles before being trapped at a suitable defect site where there even can build-up larger agglomerates covering wider areas of the R(GO) support. This process will be favored by higher precursor concentrations. However, it also explains the formation of agglomerates at low Pd precursor concentrations, as for example seen in the upper right corner of Figure S2.2 (c). Thus this mechanism seems to provide a somewhat more likely explanation for the experimental facts.

Summarizing: Small sized nanoparticles with average size of 4 nm are formed due the interaction with functional oxygen groups on the initial GO support. This is independent of the used precursor amount. However, larger-sized nanoparticles or agglomerates, which additionally can be observed, originate from Pd nanoparticles which are not anchored on free-oxygen groups. This type of initial Pd nanoparticles are highly mobile and prone to create larger particles before trapped at a defect site where eventually they can form agglomerates covering even wider zones of the GO support. The formation of these larger nanoparticles indeed is favored by higher amounts of initial Pd precursor amounts. However, at the same time the possibility of forming larger-sized nanoparticles and agglomerates strongly depends as well on the "quality" of the initial

GO support material, i.e. the number/density of functional oxygen groups and topological defects. The lower the number/density of functional oxygen groups and topological defects, so more likely is the formation of larger nanoparticles and agglomerates. This is as can be seen by in the following section S2.5, where RGO was used as starting support material.

S2.5. TEM results of Pd-NP/RGO from $Pd_2(dba)_3CHCl_3$ precursor

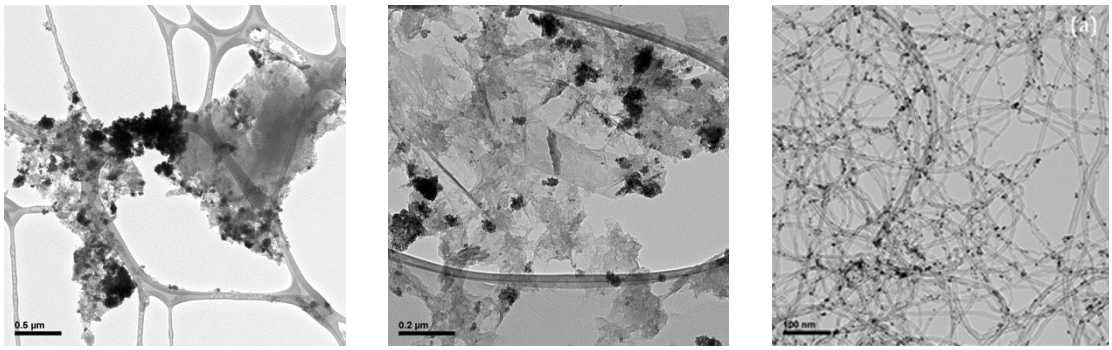

a) b) c)

Figure S2.4 TEM images of hybrid materials synthesized from precursor $Pd_2(dba)_3CHCl_3$ in toluene: (a, b) Pd-NPs/RGO and (c) Pd-NPs/MWCNTs.

Figure S2 shows TEM images of hybrid materials synthesized form precursor $Pd_2(dba)_3CHCl_3$ in toluene using the route described in S1.4. In contrast to the Pd-NPs/RGO material prepared from the $Li_2[PdCl_4]$ precursor larger Pd tends to form larger agglomerates about 20 nm not uniformly distributed on the RGO sheets, which also seem to have a more degenerated aspect. However, the initial starting conditions of the two methods are not comparable and there is space for improvement. Especially in light of results obtained using this precursor for MWCNTs and resulting Pd-NP/MWCNT composites. Here a homogeneous distribution of Pd-NPs with sizes of 4 nm well-supported on CNTs was obtained (Figure S1 c). Although functional groups are absent in the used MWCNTs, curvature and other topological defects may

contribute to a reduced mobility of Pd-NPs thus contributing to avoid clustering. On the other hand, the results obtained for RGO may point out that this precursor route either is not yet fully adapted to obtain nanoparticles of small diameter firmly attached to RGO or, due to a lower degree of topological surface defects, is inherently prone to forming larger clusters of nanoparticles on its surface.

S2.6 XRD results of Pd-NP/RGO from $Pd_2(dba)_3CHCl_3$ precursor

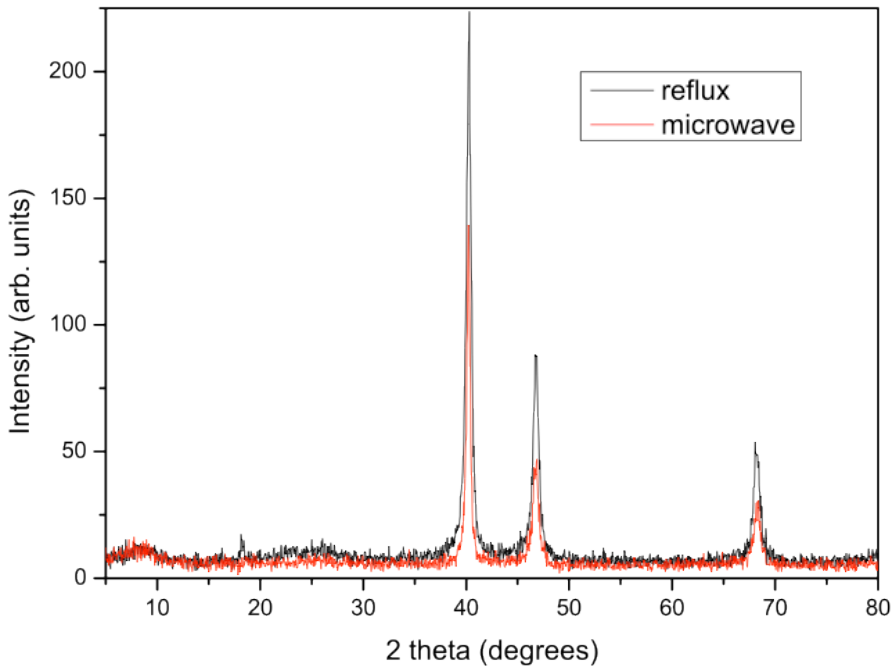

Figure S3. X-ray diffractograms of Pd-NPs/RGO material prepared from $Pd_2(dba)_3CHCl_3$ precursor under reflux and short time microwave process.

The three dominant peeks in Figure S3 at about 40 º, 47 º and 68 º correspond to the (111), (200) and (220) Bragg reflections of face-centred cubic Pd. In contrast to the Pd-NPs/RGO material prepared from $Li_2[PdCl_4]$ precursor, the peaks are of much higher intensity with respect to the underlying RGO background (indicated by the weak and broad peak at about 25 º). Furthermore the smaller FWHM indicates larger crystallite

sizes, probably related to the formation of larger Pd clusters, as also seen in TEM (see Figure S.1).

S2.7 Specific surface area of the Pd-NP/RGO hybrid material

Specific surface area of the catalyst was determined from nitrogen adsorption isotherms (BET) measurements for the RGO support material.

a) b)

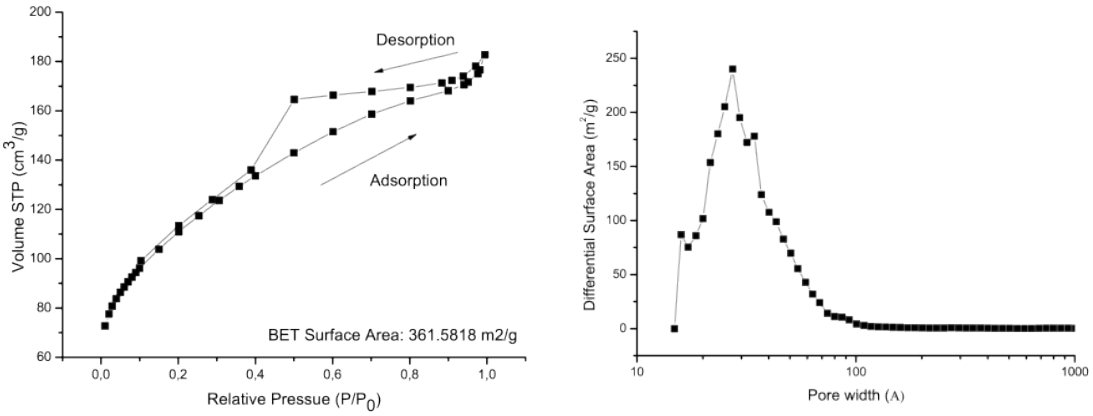

Figure S4. (a) Nitrogen adsorption isotherms of RGO support material. (b) Differential surface area as a function of pore width.

The nitrogen adsorption isotherm of the RGO support material in Figure 4a reveals a BET surface area of 361 m^2/g. Being of Type 4 it indicates the presence of micro and mesopores. The resulting pore size distribution shown in Figure 4b clearly reveals the dominance of small sized mesopores with a maximum at about 3 nm. These results are in-line with values reported in literature[10], but still below the theoretical value of 1700 m^2/g for isolated RGO sheets.[11] due to agglomerations and partial overlapping of reduced sheets.[10]

Taking into account the experimentally determined BET surface area of RGO, the average Pd-NPs diameter as determined by TEM, and the mass of Pd and RGO of the overall catalyst system the specific surface area of the overall Pd-NPs/RGO catalyst system of 315 m^2/g was obtained. The corresponding calculations and resulting values are summarized in Table S1 (please note that the synthesized quantities of the overall catalyst material were not sufficient for carrying out reliable BET measurements on the Pd-NPs/RGO material itself). In addition to the values based on the experimental BET results for RGO shown in the second column of Table S1, for the sake of comparison, the last column provides values based on the surface area for an ideal sheet of RGO of 1700 m^2/g.[11]

Table S1. Estimation of specific surface area (SSA) of the Pd-NPs/RGO hybrid

Specific surface area (SSA) of RGO (m^2/g)	360	1700^{+++}
Mass of RGO (g)	35	35
Surface area of 35 mg RGO (m^2)	12.5	59.5
Average diameter of Pd NPs (nm) according to TEM analysis	4	4
Average surface area of Pd NPs (nm^2)	50	50
Average catalytically active surface area of Pd NPs $(nm^2)^+$	40	40
Total number of isolated Pd NPs covering surface area of 35 mg GO (m^2)	3×10^9	6×10^9
Surface area of total number of isolated Pd NPs (m^2)	1.5×10^{-7}	3×10^{-7}
Mass of Pd-NPs/RGO hybrid (mg)	40	40
SSA of Pd-NPs/RGO hybrid $(m^2/g)^{++}$	315	1490
Difference SSA hybrid and GO (m^2/g)	45	210
Percentage of SSA difference (%)	12.5	12.5

$^+$Value taking into account that only 80% of Pd are in catalytically active Pd^0 state (according to XPS results).

$^{++}SSA_{hybrid}$ = (surface $area_{RGO}$ – surface $area_{Pd}$)/$mass_{hybrid}$.

$^{+++}$ last column corresponds to calculations for an ideal surface area of a single RGO sheet of 1700 m^2/g.[11]

References

1. W. S. Hummers and R. E. Offeman, *Journal of the American Chemical Society*, 1958, **80**, 1339.
2. X. L. Li, G. Y. Zhang, X. D. Bai, X. M. Sun, X. R. Wang, E. Wang and H. J. Dai, *Nat. Nanotechnol.*, 2008, **3**, 538-542.
3. C. Vallés, P. Jiménez, E. Muñoz, A. M. Benito and W. K. Maser, *The Journal of Physical Chemistry C*, 2011, **115**, 10468-10474.
4. C. Vallés, J. D. Núñez, A. M. Benito and W. K. Maser, *Carbon*, 2011, **50**, 835-844.
5. M. Cano, A. M. Benito, W. K. Maser and E. P. Urriolabeitia, *Carbon*, 2011, **49**, 652-658.
6. M. Cano, A. M. Benito, W. K. Maser and E. P. Urriolabeitia, *New Journal of Chemistry*, 2013, **37**, 1968-1972.
7. C. Nethravathi, E. A. Anumol, M. Rajamathi and N. Ravishankar, *Nanoscale*, 2011, **3**, 569-571.
8. J. A. Rodríguez-Manzo, O. Cretu and F. Banhart, *ACS Nano*, 2010, **4**, 3422-3428.
9. B. E. Warren, *X-ray diffraction*, Dover Publications, Inc., New York, 1969.
10. S. Stankovich, D. A. Dikin, R. D. Piner, K. A. Kohlhaas, A. Kleinhammes, Y. Jia, Y. Wu, S. T. Nguyen and R. S. Ruoff, *Carbon*, 2007, **45**, 1558-1565.
11. T. Szabó, E. Tombácz, E. Illés and I. Dékány, *Carbon*, 2006, **44**, 537-545.